

On the links between the radio flux and magnetodisc distortions at Jupiter.

Philippe Louarn¹, Margaret G. Kivelson², William S. Kurth³

1 Université de Toulouse, IRAP, CNRS, UPS, Toulouse, France

2 Johns Hopkins University Applied Physics Laboratory, Laurel, Maryland, USA

3 Department of Physics and Astronomy, University of Iowa,, Iowa City, Iowa,, USA

Abstract. Using measurements of the Galileo magnetometer and plasma wave instrument, it is shown that the flux of the jovian auroral radio emissions is correlated with the azimuthal component of the magnetic field (B_ϕ) measured in the plasma disc, the situations of large magnetic twist of the disc (large ΔB_ϕ , the difference between the measured and the model field) corresponding to enhanced radio intensities (frequency > 300 kHz). For the 4 orbits discussed here (3 in the post mid-night and one in the pre mid-night sector), representing ~ 44 days of observations, from 25 to 85 jovian radius in the magnetodisc, the radio intensity observed during periods of small radial current ($\Delta B_\phi < 1$ nT) is typically a factor of 5 to 10 smaller than that observed at large radial current ($\Delta B_\phi > 5-6$ nT). It is proposed that these variations are the direct consequences of enhanced magnetosphere/ionosphere coupling current systems linked to episodes of larger outward mass outflows in the disc, resulting in larger parallel currents and, thus, in enhanced auroral activity. The application of Hill's model shows that the observed variations of B_ϕ can be explained by increasing the mass outflow rate from ~ 150 kg/s (quiet periods) to more than 2 tons/s ('energetic' events), for Pedersen conductance ranging from 0.1 to 1 S. This is consistent with the canonical values given in the literature. It is estimated that these modulations of the mass flow rates lead to variations of the power dissipated in the disc from $\sim 10^{14}$ to 10^{15} W due to the torque exerted by the magnetic coupling with Jupiter's ionosphere, with a conversion rate into the power radiated by the radio waves of the order 10^{-6} .

1-INTRODUCTION

This is the author manuscript accepted for publication and has undergone full peer review but has not been through the copyediting, typesetting, pagination and proofreading process, which may lead to differences between this version and the Version of Record. Please cite this article as doi: [10.1002/2016JA023106](https://doi.org/10.1002/2016JA023106)

The dynamics of Jupiter's magnetosphere is organized mainly by the way the plasma resulting from the ionization of the gases produced by Io's volcanic activity is transported radially and driven in rotation by its magnetic coupling with Jupiter [Bagenal and Sullivan, 1981; Hill *et al.*, 1983; Belcher, 1983; Krimigis and Roelof, 1983; Vasyliunas, 1983]. As initially studied by Hill [1979], this rotating magnetosphere is characterized by a large scale magnetosphere-ionosphere (M-I) coupling current system that transfers angular momentum from Jupiter to the outflowing plasma which contributes to maintaining the magnetodisc near corotation. This current system consists of an equatorward directed ionospheric Pedersen current that links to a radial current in the disc, and closes through upward field-aligned current in the outer magnetosphere (Figure 1). Combined with the equatorial magnetic field, the radial current exerts a $\mathbf{J} \times \mathbf{B}$ torque on the disc and acts to maintain its partial corotation. Some important characteristic features of this system are the bending back of the magnetic field lines out of the meridian plane [Khurana *et al.*, 2004; Krupp *et al.*, 2004] and the existence of a bright permanent auroral oval associated with the region of upward directed currents [Hill, 2001, Grodent *et al.*, 2003, Clarke *et al.*, 2004, Nichols *et al.*, 2009].

Hill's initial model has been improved to include realistic magnetic models [Pontius, 1997, Cowley and Bunce, 2001, Cowley *et al.*, 2002] and to include the effects of the radial mass flow (\dot{M}) and the effective Pedersen conductivity (Σ) on the angular velocity radial profile [Nichols and Cowley, 2003, 2004]. The consequences of field-aligned potential differences in the upward current region [Nichols and Cowley, 2005, Ray *et al.*, 2010] and the inclusion of anisotropic magnetospheric pressures [Nichols, 2011, Nichols *et al.*, 2015] have also been considered. A common feature of these models is that the radial equatorial current and, thus, the resulting magnetic field bend-back (or the magnetic twist of the disc) are directly associated with the mass outflow \dot{M} , with a radial profile of angular velocity that also depends on the Pedersen conductance, Σ . The model systematically shows that larger mass outflows lead to larger delays from corotation, enhanced M-I current systems and more intense upward-directed field-aligned currents.

According to the current knowledge of auroral processes, variations in the M-I coupling efficiency should have strong observational consequences. As inferred by observations made at Earth [Evans, 1974; McFadden *et al.*, 1999; Ergun *et al.*, 2000a] parallel electric fields form in regions of upward field-aligned currents, leading to parallel particle accelerations. Knight [1973] formulated how the current density is linked to the field-aligned potential in a magnetic mirror geometry [see also Chiu and Schutz, 1978; Lyons, 1980]. This concept was applied in the jovian context by Nichols and Cowley, [2005] and adapted to consider the large centrifugal potentials by Ergun *et al.* [2009] and Ray *et al.* [2009, 2010, 2015], with the conclusion that the canonical mass outflows ($\dot{M} \sim 1000 \text{ kg/s}$) may explain the development of field-aligned potentials of several 10s of kV and the generation of the main auroral oval.

The auroral particle acceleration process is also intimately associated with the generation of plasma waves, including radio emissions [Gurnett, 1974; Roux *et al.*, 1993]. More specifically, as shown from *Viking* and *FAST* spacecraft observations at Earth, the parallel electron acceleration combined with the conservation of the first adiabatic invariant creates plasma conditions that are favorable to the generation of radio waves by the cyclotron maser instability [Louarn *et al.*, 1990; Ergun *et al.*, 1998, 2000b; Delory *et al.*, 1998]. Consequently, situations of enhanced auroral activity should lead to intensifications of the auroral kilometric radiation (AKR). This has been verified by Kurth and Gurnett [1998], with the proof that the AKR intensity is a good proxy of auroral activity. Similar scenarios most probably apply at Jupiter and Saturn [Zarka, 1998; Gurnett *et al.*, 2002; Kurth *et al.*, 2005; Lamy *et al.*, 2013]. One may thus expect that the intensity of the auroral radio emissions at Jupiter - mostly at hectometric and decametric wave length (the so-called HOM and DAM) - and Saturn (the kilometric radiation or SKR) are also good proxies of auroral activity in general and, more specifically, of the intensity of the upward field-aligned currents.

In the present article, we explore this scenario linking mass outflow to the intensity of radio emissions. We analyze Galileo data to examine whether the disc magnetic twist is correlated with the radio intensity. As sketched in Figure 1, our goal is to relate variations of the magnetic

configuration of the disc (its twist, in particular) to modulations of overall auroral activity, as indicated by the power in radio emissions. The principle is simple. Increases of the azimuthal magnetic field in the disc are inherently associated with the strength of the radial current in the disc, which requires an enhanced M-I coupling current system. This should be associated with more intense auroral activity and powerful auroral radio flux. According to Hill's model, this variability should reflect modulations in the mass outflow rate.

This interpretation assumes that the disc magnetic twist is predominantly linked to internal processes which, given the importance of the rotation and mass loading effects at Jupiter, appears to be the most natural. However, this model requires some comments. The Galileo observations have indeed revealed that the magnetosphere presents a significant dawn/dusk asymmetry, which has been interpreted as a consequence of its interaction with the solar wind [Khurana, 2001, Khurana *et al*, 2004]. A larger magnetic bend-back is observed in the post-midnight and morning sector so that the magnetic twist cannot be systematically attributed to the rotation and mass loading effects only. Both solar wind variations and magnetopause processes may perturb the azimuthal field [Delamere *et al*, 2015 a, b] with likely a positive correlation with the radio intensity since it is established that the Jovian radio emissions are, in part, correlated to the solar wind perturbations (see for example, Genova *et al.*, [1987], Gurnett *et al.*, [2002], Prangé *et al.*, [2004], Hess *et al.*, [2014]).

It appears difficult to disentangle external from internal processes. One solution is to consider that the relative importance of both effects certainly varies with the distance from the magnetopause and that the external effects on the magnetic bend-back varies with Local Time (LT). It is expected to be maximum near the magnetopause, in the morning sector and, comparatively, minimum and even inverse in the evening sector. Since we are essentially interested by internal effects, we thus consider observations made at moderate distances from Jupiter, in the disc 'proper', from 20 to 60-70 Jovian radius (R_J), at ± 3 hours from midnight local time, then relatively far from the magnetopause. In section 2, we first consider observations obtained in the post-midnight sector and establish the correlation between the magnetic twist

(bend-back perturbations) and the radio flux. However, we also discuss observations performed in the evening sector that shows the same phenomenology, with a larger magnetic bend-back in periods of intense radio flux. This is not the expected effect of external perturbations and supports the hypothesis of dominant internal effects.

In section 3, we compare the predictions of Hill's model to the measured azimuthal magnetic field. This is used to infer the range of parameters (\dot{M} and Σ^*) that are consistent with the observations. The energetic consequences are discussed in section 4, with estimates of the power dissipation in the M-I current system and the conversion rate into particle acceleration and radio flux.

2-OBSERVATIONS

2-1 DETAILED ANALYSIS OF A RADIAL DISC CROSSING

In this section, we describe the observations performed during a particular radial crossing of magnetodisc to show the possible relationship between the radio flux and the magnetic twist of the disc. The wave and magnetic field measurements performed from DOY 77 to 92, 1997, on an inbound Galileo orbit, from ~ 85 to 25 Jovian radius (R_J) in the post-midnight sector (from 3 to 4 LT), are displayed in Figure 2 (see *Kivelson et al.* [1992] and *Gurnett et al.* [1992], for descriptions of the MAG and PWS instruments).

The high frequency part of the wave spectrogram is displayed in panel (a). It shows two Jovian radio emissions: (1) the broad band hectometric 'HOM' emission above ~ 300 kHz and (2) the narrow band kilometric 'nKOM' emission from 50 to 200 kHz. As already mentioned, 'HOM' is an analogue of AKR at Earth (*Zarka* [1998]). It is most certainly generated by the cyclotron maser instability along auroral magnetic field lines, with a global flux that gives a proxy of the auroral activity. The 'nKOM' has a very different origin. It is organized in bursts

with an ~ 10 hour periodicity, coming from sources that rotate in the outer Io torus at $\sim 8-9 R_J$ [Reiner *et al.*, 1993].

In panel (b), the spectrogram, restricted to frequencies below 10 kHz, shows the continuum radiation and various locally emitted plasma waves. The low frequency cut-off in the continuum is at the plasma frequency. The ~ 5 -hour periodicity corresponds to the regular crossings of the plasma sheet. The variations are particularly large when Galileo approaches Jupiter closer than $60-70 R_J$, with oscillations from $\sim 1-2$ kHz (meaning electron density $\sim 0.01-0.05 \text{ cm}^{-3}$) in the central sheet to less than 100 Hz ($< 10^{-4} \text{ cm}^{-3}$) in the lobe regions.

The HOM intensity shown in panel (c) is obtained by integrating the spectral intensity from 300 kHz to 5.6 MHz. It is normalized to $10 R_J$, using a correction for the square of the Galileo/Jupiter distance. A sliding 1-hour window average is applied to eliminate short scale fluctuations. Since the emission is strongly modulated by the planet's rotation, we also show the maximum intensity (in blue) and the average intensity (in red), measured over each Jovian rotation. They will be denoted mI and aI , respectively, and expressed in $(\text{V/m})^2$.

One notices that the HOM intensity may vary by a factor as large as 10 over time scales of a few Jovian rotations. As discussed in the introduction, this likely reflects variations in auroral activity and, by extension, in the intensity of the M-I current system coupling. In the present case, the activity would thus be particularly important on DOY 78, 82, 86 and 90 (red line) when HOM bursts are observed. This corresponds to the occurrence of 'energetic events' as described by Louarn *et al.*, [1998, 2000, 2001]. Their phenomenology includes the simultaneous observations of (1) a burst in the intensity of HOM and a broadening towards lower frequencies, (2) the formation of a new source of nKOM, seen at a different system III longitude than the previous ones and (3) fluctuations in the cut-off frequency of the continuum emission that can be interpreted as local plasma density perturbations. Note that 'simultaneously' means here 'within a Jovian rotation' since the emission beaming and the rotation have to be considered. The red lines show the first indication of the events; it is not necessarily the HOM burst itself and may be the low frequency extension of the HOM or the new nKOM source. These events are often followed

by sequences of sudden thickening followed by progressive thinning of the plasmadisc, as seen after \sim DOY 78.3 and 82.5 (see *Louarn et al.*, [2000] for details) that can be interpreted as variations in the plasma content of the magnetodisc. They are also systematically linked to energetic particle injections seen in the outer part of Io's torus [*Mauk et al.*, 1999; *Louarn et al.*, 2001, 2014].

In panels (d) and (e), the absolute values of the radial (B_r) and the azimuthal (B_ϕ) magnetic components are plotted. They are compared to Khurana's model (in red), calculated using the code available at the web site of the Laboratory for Atmospheric and Space Physics [see details in *Khurana et al.*, 2004]. Absolute values are used for a better visualization of the long term variations. In reality, B_r is alternatively positive and negative, according to the North/South position of Galileo with respect to the current sheet, and B_ϕ varies in antiphase with B_r , as expected if the magnetic twist is consistent with a lag from corotation.

B_r and B_ϕ generally present well defined 'square' profiles, with short intervals where they decrease to zero as Galileo crosses the center of the current sheet. The disc is thus relatively thin so that Galileo regularly enters into the lobes. This is also consistent with the modulations of the upper hybrid frequency seen in panel (b). The availability of measurements well above or below the center of the current sheet is useful for obtaining reliable estimates of the total current flowing in the sheet from the lobe-to-lobe variations of the magnetic field.

The correlation between the radio flux and the magnetic field is particularly obvious from DOY 84 to 90, as Galileo approaches Jupiter from ~ 70 to $\sim 40 R_J$. The radio intensity increases by one order of magnitude from $mI \sim 0.3 \cdot 10^{-7}$ and $aI \sim 0.1 \cdot 10^{-7} \text{ (V/m)}^2$ on DOY 84 to $mI \sim 2.7 \cdot 10^{-7}$ and $aI \sim 1.1 \cdot 10^{-7}$ on DOY 86.5. This maximum corresponds to the energetic event. The flux then decreases to $mI \sim 0.6 \cdot 10^{-7}$ and $aI \sim 0.2 \cdot 10^{-7}$ until DOY 90, just before the next energetic event. Over the same time period, B_r and B_ϕ rise from their model values at DOY 84 (respectively 7 and 2.5 nT) to reach maxima at the energetic events (respectively 13 and 8 nT, meaning ~ 5 nT above the model). They then return close to model values at DOY 90.

The same radio- B_ϕ correlation is observed in the energetic events occurring on DOY 90 and, although less obvious, DOY 82. Thus, B_ϕ increases from ~ 4 nT on DOY 89.5 to 9 nT on DOY 91.5 (~ 5 nT above the model) as the radio intensity also increases from $mI \sim 0.5 \cdot 10^{-7}$ to $3 \cdot 10^{-7}$ (V/m)². Similarly, B_ϕ is close to 5 nT on DOY 82.2 (~ 3 nT above the model value) and decreases to 2.5 nT on DOY 84.5, when simultaneously the radio intensity decreases from $mI \sim 3.9 \cdot 10^{-7}$ (V/m)² to $0.3 \cdot 10^{-7}$ and aI from $0.9 \cdot 10^{-7}$ to $0.1 \cdot 10^{-7}$.

One can also study the correlations with the magnetic bending angle: $\zeta = \text{atan}(B_\phi/B_r)$ and the normalized twist: $Tw = B_\phi/(r \cdot B_r)$, shown in panel (e) and (f). The normalized twist is often used in the literature since it corrects for the tendency of the magnetic spiral angle to increase linearly with radial distance. For convenience, we again present the absolute values of these quantities, both being negative in reality for the whole time period. Since these quantities fluctuate considerably near the center of the current sheet, values calculated with small B_r ($B_r < 2$ nT) are excluded. The small horizontal black bars in the plots are 2-hour averages, calculated between successive sheet crossing, when Galileo is expected to be well above or below the current sheet. The red dashed lines show the model values.

The quasi-linear increase of the bending angle with distance to Jupiter is obvious in panel (e) and well reproduced by the model. Superposed on this regular variation, the bending angle shows increases of more than 10° that are correlated with the energetic events. For example, for the period DOY 84-90, the bending angle is close to the model value on DOY 84.0 ($\sim 18^\circ$) when the radio intensity is very low; it then reaches $\sim 25^\circ$ ($\sim 9^\circ$ above the model) on DOY 86.5 when the energetic event occurs, before a slow return to the model value on DOY 90 as the radio intensity decreases. Similar, but weaker, responses are observed around days 82 and 90, with bending angles about 5° above the model values when the radio intensity maximizes and close to the model value when mI decreases below $1 \cdot 10^{-7}$ (V/m)².

The correlation with the normalized twist is also clear (panel g). The model value is ~ 0.0055 (with distances expressed in R_J) and only slowly varies with radial distance. This is about the observed value at DOY 84, when the radio intensity is minimal. It then increases to ~ 0.011 at

86.5, before a slow return to the model value on DOY 90. In general, values greater than 0.008 are observed at or slightly after each event. One can also notice that the normalized twist increases after the first event, on DOY 78, when the radio flux also intensifies. This variation is harder to detect from the bending angle.

To be complete, one may notice that the radio flux also correlates with the total magnetic field. For example, at DOY 86.5, the peak in the radio flux is observed when the total field is also at a local maximum or, more precisely, when the difference with the model field is maximum. This particular event has been studied by *Ge et al.*, [2007] who proposed an analogy with the substorm ‘growth phase’.

2-2 OTHER EXAMPLES IN THE POST MID-NIGHT SECTOR

We extend the previously reported observations by first analyzing two additional examples of periodic encounters of the plasma sheet along a largely radial pass through the disc (Figure 3), corresponding to the periods DOY 166-176, 1997 and 251-259, 1997, in the post-midnight sector (from 3 to 5 LT). The observations are plotted as functions of radial distance, with the time (DOY) indicated at the top of the panels. Two events occur during the first time period, at DOY 171 and 175, at distances from Jupiter ~ 55 and $30 R_J$. During the second time period, an event occurs at DOY 256, at a distance of $\sim 48 R_J$.

The interval DOY 170-175 provides a particularly good example of link between the radio flux and the magnetic twist. This 5-day period corresponds to a Jupiter approach from ~ 65 to $30 R_J$. At DOY 170, the radio intensity is at minimum: $mI \sim 1.10^{-7}$, $aI \sim 0.4 \cdot 10^{-7} \text{ (V/m)}^2$ when B_ϕ , the bending angle and the normalized twist are close to the model. B_r is $\sim 20 \%$ above the model. The radio intensity then systematically increases to reach a local maximum at DOY 171.6: $mI \sim 5.10^{-7}$, $aI \sim 1.5 \cdot 10^{-7}$. During the same interval, B_ϕ also increases to a local maximum ($\sim 11 \text{ nT}$, thus $\sim 7 \text{ nT}$ above the model), as does the bending angle ($\sim 30^\circ$ or $\sim 14^\circ$ above the model) and the normalized twist (~ 0.012 or ~ 0.0065 above the model). Both B_r and the total field also increase

to ~30 % above the model. The radio intensity then remains large with a decreasing trend interrupted by partial recoveries, until DOY 174.4, with $mI \sim 2.1 \cdot 10^{-7}$, $aI \sim 0.9 \cdot 10^{-7}$. The total field, B_r and B_ϕ decrease for about 20 hours following the event, with values approaching the model, but again increase to a plateau until 174.4, with $B_\phi \sim 8$ nT, a bending angle $\sim 22^\circ$ ($\sim 8^\circ$ above the model) and a normalized twist ~ 0.009 (~ 0.0055 above the model). At 174.4, the radio intensity sharply decreases, with $mI \sim 0.8 \cdot 10^{-7}$, $aI \sim 0.2 \cdot 10^{-7}$, until the next event at 175.3. Simultaneously, B_ϕ , the bending angle and the normalized twist also decrease to reach values close to but slightly larger than the model, and, as in the start of the plotted interval, the field magnitude and B_r remain somewhat larger than the model predictions.

A similar radio-twist correlation is observed from DOY 251 to 259. Most of the time, B_r , B_ϕ , the bending angle and the normalized twist are close to the model values and the radio intensity is relatively low: $mI < 1 \cdot 10^{-7}$ and $aI < 0.3 \cdot 10^{-7}$. However, from DOY 255.5 to 257.2, at $44 - 53 R_J$, the magnetic field becomes $\sim 30\%$ larger than the model, with a $\sim 10^\circ$ increase of the bending angle. This significant enhancement of the magnetic twist is well correlated with an intensification of the radio flux that starts at 255.7, from $mI \sim 0.4 \cdot 10^{-7}$ and $aI < 0.2 \cdot 10^{-7}$ to peak at 256.2 with intensities 4-5 times larger: $mI \sim 1.6 \cdot 10^{-7}$ and $aI \sim 0.6 \cdot 10^{-7}$. This more intense radio flux is then observed for ~ 20 hours during which time both the bending angle and the twist remain $\sim 25-30\%$ above the model values.

In conclusion, the observations described in Figure 2 and 3 appear to be consistent with the model sketched in Figure 1. The time periods of large B_ϕ and, thus, of strong radial currents flowing in the disc, are apparently well correlated with enhancements in the auroral radio flux. This suggests that they are also associated with intensifications of the parallel currents connecting the disc to the ionosphere and, thus, likely to correlate well with strong auroral activity.

2-3 CORRELATION BETWEEN RADIO INTENSITY AND TWIST

Our purpose is now to quantify the correlation between the radio flux and the magnetic twist or B_ϕ . We thus analyze observations made in the disc ‘proper’, from 30 to 70 R_J , and we determine the radio intensity (mI and aI) as functions of B_ϕ , and the twist (Tw). This is done by first identifying each incursion into either the northern or southern lobe, defined as the time interval separating two successive crossings of the plasma sheet. Periods of +/- 2 hours from the centers of these time-intervals are used to determine the maximal and averaged values of B_ϕ and Tw , and periods of 5 hours (~one half Jovian rotation) are used to determine mI and aI . Series of 30 to 40 points are then obtained for successive portions of the selected orbits, corresponding to a time cadence of ~5 hours.

The plots in Figure 4 show the radio intensity as a function of the difference between the measured and the model twist: $\Delta Tw = Tw_{measured} - Tw_{model}$. The green lines show the linear fits:

$$aI = aI_0 + \Lambda \left(\frac{B_\phi}{\rho B_r} - \left(\frac{B_\phi}{\rho B_r} \right)_{mod.} \right) = aI_0 + \Lambda \Delta Tw \quad (1)$$

Although the points are somewhat scattered, it is clear that the radio flux tends to increase with ΔTw . The scatter is reduced when the averaged fluxes are considered (rightmost plots). One may notice that considering individually each orbit, the average flux at $\Delta Tw \sim 0$ is systematically below the flux at $\Delta Tw > 0.004$, i.e. when the twist is almost twice the model value.

Fits of equation (1) to the data in Figure 4 give typical values: $aI_0 \sim 1.5 \cdot 10^{-8} \text{ (V/m)}^2$ and $\Lambda \sim 1.25 \cdot 10^{-5}$. In this formula, aI_0 can be interpreted as the HOM intensity of the quiet magnetosphere, normalized to 10 R_J . The typical value of Λ corresponds to an increase of the average radio intensity by a factor 5 from the low twist intervals (when the twist is close to the model value or $Tw \sim 0.005$) to the large twist intervals ($Tw > 0.01$). When applied to the maximal intensity (mI), the linear fit shows that Λ varies from $1.8 \cdot 10^{-5}$ to $3.9 \cdot 10^{-5}$ with the orbit, the latter value indicating that the maximum HOM intensity may increase by a factor 15, from small to large twist situations.

The lowermost plots of Figure 4 include measurements from all of the different orbits. The tendency for the flux to increase with twist is still present. However, the typical fluxes differ from one orbit to another in a way that is not described by the twist only. For a given twist, the flux measured during the period 168-171 is systematically larger than during 253-258. To explain this observation, one may notice that B_r at the same distance is generally larger during the first period than the second one (B_r is several nT above the model during the first period and close to the model during the second one). To get the same twist, larger B_ϕ are then needed for the first period, meaning larger parallel current and, thus, more radiation flux.

This possible mixed B_r/B_ϕ effect is not present in Figure 5, where the averaged radio intensity is plotted as a function of the difference between the averaged B_ϕ (left) or maximal B_ϕ (right) and the model value. The linear fits, similar to (1), are shown with the normalized chi-squared value indicated in each plot. One again observes the clear correlation between the radio intensity and B_ϕ , with intensities generally below $2 \cdot 10^{-8}$ when for $\Delta B_\phi < 1$ nT and above 10^{-7} for $\Delta B_\phi > 6$ nT. The slope of the fit is typically $0.12 \cdot 10^{-7} \text{ (V/m)}^2/\text{nT}$, with an intensity of $\sim 10^{-8}$ for $\Delta B_\phi = 0$. The use of the averaged B_ϕ or the maximum B_ϕ does not significantly change the quality of the fits. This may be an indication that the radial current flows over a large range of local time or that possible intensifications in longitude of radial current have little effect on the global radio flux.

Similar analyses have also been performed considering the total magnetic field (B_T) and the radial component (B_r) only (Figure 6). In general, more scattered plots are obtained, with larger chi-squared values (by typically 0.06 to 0.1) than with ΔB_ϕ . The comparison with the plots in Figure 5 (plots for ΔB_ϕ) clearly shows a significant loss of correlation between ΔB_T or ΔB_r and the radio flux. One can even consider that there is no correlation between the radio flux and B_T or B_r for modest increases above the model values ($\Delta B_T, \Delta B_r < 4$ nT) and that the tendency of global increase of the radio flux is observed for situations of large current only ($\Delta B_T, \Delta B_r > 5$ nT).

In conclusion, this quantitative analysis confirms the observations described in the previous sections. For the three orbits discussed here, representing 34 days of observations, the radio

intensity observed during periods of small radial current ($\Delta B_\phi < 1$ nT) is typically a factor 5 to 10 smaller than the one observed at large radial current ($\Delta B_\phi > 5-6$ nT). The comparison with ΔB_T and ΔB_r does not show convincing correlations with the radio flux, except that situations of large total or azimuth currents ($\Delta B_T, \Delta B_r > 5$ nT) generally correspond to large fluxes (fluxes larger than the averaged measured during the considered orbit). This analysis shows that increase in B_ϕ and, thus, in parallel current is what is correlated with the radio flux with, probably, the tendency that B_ϕ and B_r (thus, the radial and azimuthal currents) increase together in cases of particularly strong activity.

2-4 EXAMPLE IN THE PRE MID-NIGHT SECTOR

In Figure 7, we present the period DOY 178-188, 1997 corresponding to the outbound radial disc crossing that follows the first example given in Figure 3. Galileo is now in the evening sector, at 18 to 23 LT and 20 to 80 R_J . The panels (a) and (b) show the HOM observations, using the same format as in Figure 2. A first event occurs on DOY 179.5, with a large radio intensity seen till DOY 182.5, and a moderate one on DOY 183.5. In panels (c) and (d), B_r and B_ϕ are displayed and compared with the model (in red). If B_r is generally close to the model even if it presents less defined square-shaped variations, B_ϕ shows significant variations from the model with the same correlation with the radio intensity as described in the post mid-night sector. In absolute value, B_ϕ is ~ 10 nT above the model, at DOY 179, when the first event occurs. Then, after a short decrease on DOY 180, it remains ~ 5 nT larger than the model until DOY 182.5, during the period of the maximum radio flux. After DOY 183, it returns to close to the model as the radio flux decreases.

Due to large short scale magnetic fluctuations, the instantaneous tilt angle (shown in cyan in Figure 2 and 3) is very spiky. We prefer to estimate the tilt angle by averaging B_r and B_ϕ over 3 hour periods centered between each crossings of the current sheet center. In panel (e), these

estimates are shown in blue and compared with the model. Contrary to Figures 2 and 3, the actual values of the magnetic field and tilt angle are displayed since one may expect to observe both bend-back and bend-forward perturbations (respectively, negative and positive tilt angle) in the evening sector. As already mentioned, only bend-back perturbations were observed in the previous examples.

In panel (e), one notices the existence of a few short periods of bend-forward perturbations. They are, however, never observed when the azimuthal perturbations are large. Most of the time the tilt angle is negative and shows bend-back perturbations up to $5\text{-}10^\circ$ larger than the model when the radio flux is intense, as before DOY 183. These large bend-back perturbations are observed from $20\text{-}60 R_J$, between 18 to 22 LT. Later, a bend-back is still observed but smaller than the model values.

In overall, the phenomenology thus remains unchanged: the bend-back perturbations are correlated with the radio intensifications. Since the B_ϕ perturbations that would be induced by solar wind effects, due for example to larger dynamic pressure, are expected to bend forward in the evening sector, this observation supports the hypothesis of a dominant role of the internal processes in the magnetic twist, at least at distances smaller than $\sim 60 R_J$. This justifies an interpretation based on Hill's model, as developed in the next sections.

3- MODEL AND INTERPRETATION

3.1- BASIC EQUATIONS

In this section, we summarize the classical model of the M-I current system coupling first proposed by *Hill* [1979, 2001] and *Vasyliunas* [1983] and later extended by *Pontius* [1997], *Cowley et al.* [2001, 2002], *Nichols et al.* [2003, 2004, 2005, 2011, 2015] , *Ray et al.* [2009, 2010]. The formulation developed below follows *Nichols et al.* [2004, 2005].

The magnetic field is specified by a flux function $F(\rho, z)$ defined by $\vec{B} = (1/\rho) \vec{\nabla} F \times \vec{e}_\varphi$, where ρ is the distance from the magnetic axis (assumed to be co-aligned with the rotation axis as a first approximation), z the distance from the magnetic equator, φ the azimuthal angle. The condition $F(s) = \text{constant}$ (s is distance along the field line) defines a flux shell; it is used to magnetically map the ionosphere (subscript ‘ i ’) to the equatorial plane (subscript ‘ e ’) by the equation $F(s) = F_i = F_e$. Considering a pure dipole field at the ionosphere and assuming that $F=0$ on the magnetic axis, F_i is given by:

$$F_i = B_J \rho_i^2 \quad (2)$$

where B_J is the dipole magnetic field strength at the equator at the surface of the planet ($B_J = 4.26 \times 10^5$ nT). The flux in the equatorial plane is linked to the z component of the magnetic field by:

$$B_{ze} = \frac{1}{\rho_e} dF_e/d\rho_e \quad (3)$$

and for a dipole field, $F_e = B_J \rho_e^{-1}$.

Following Hill’s work, the ionosphere height-integrated Pedersen current flowing in the equatorward direction can be related to the magnetospheric angular velocity (ω) by:

$$i_p = 2\Sigma B_J \rho_i (\Omega - \omega), \quad (4)$$

where Σ is the effective height integrated Pedersen conductivity and takes into account the neutral atmosphere slippage and Ω is the jovian angular velocity. The magnetic field in the polar ionosphere is considered to be nearly vertical and equal to twice the surface field at Jupiter’s equator (B_J).

Assuming symmetry between the northern and southern ionospheres for simplicity, the current continuity equation that relates the radial current i_ρ flowing in the disc, integrated over the sheet thickness, to the Pedersen current is: $\rho_e i_\rho = 2\rho_i i_P$, so that using (2) and (4) :

$$i_\rho = \frac{4\Sigma\Omega F_e}{\rho_e} \left(1 - \frac{\omega}{\Omega}\right). \quad (5)$$

From Ampère's law, the azimuthal magnetic field (B_ϕ) just above the plasma sheet is then:

$$B_\phi = \pm 2\mu_0 \frac{\Sigma\Omega F_e}{\rho_e} \left(1 - \frac{\omega}{\Omega}\right). \quad (6)$$

The signs '+' and '-' corresponding to the northern and southern hemispheres, respectively.

The field-aligned current can be calculated from the divergence of i_ρ . Considering the northern vertical current flowing out of the disc, one gets: $j_{ze} = -\frac{1}{2\rho_e} \frac{d\rho_e i_\rho}{d\rho_e}$ and, thus:

$$\frac{j_\parallel}{B} = \frac{j_{ze}}{|B_{ze}|} = -\frac{2\Sigma\Omega}{\rho_e |B_{ze}|} \frac{dF_e \left(1 - \frac{\omega}{\Omega}\right)}{d\rho_e}. \quad (7)$$

The angular velocity ω is calculated by solving the dynamical equation that relates the temporal variation of the plasma-disc kinetic moment to the torque exerted by the current system. Assuming cylindrical symmetry, a stationary state, and noting \dot{M} the mass flux rate, the dynamical equation is (Hill, [1979]) :

$$\frac{d}{d\rho_e} (\rho_e^2 \omega) = \frac{2\pi\rho_e^2 i_\rho |B_{ze}|}{\dot{M}}, \quad (8)$$

or, substituting (5):

$$\frac{1}{\rho_e} \frac{d}{d\rho_e} \left(\rho_e^2 \frac{\omega}{\Omega} \right) = \frac{8\pi \Sigma F_e |B_{ze}|}{\dot{M}} \left(1 - \frac{\omega}{\Omega} \right). \quad (9)$$

To progress, the profile of B_{ze} needs to be specified. *Nichols and Cowley* [2004] proposed a useful combination of the Voyager-1/Pioneer 10 model of *Connerney et al.* [1981] – the CAN model, valid in the inner magnetosphere ($\rho < 25 R_J$) – and the Voyager 1 model of *Khurana and Kivelson* [1993] – the KK model, valid at larger distances in the disc:

$$|B_{ze}(\rho_e)| = B_0 \left(\frac{R_J}{\rho_e} \right)^3 \exp \left[- \left(\frac{\rho_e}{L} \right)^\alpha \right] + A \left(\frac{R_J}{\rho_e} \right)^m. \quad (10)$$

The first term in this expression is a modified dipole field and the second term is the KK model. *Nichols and Cowley* [2004] considered the KK model, with $A=5.4 \cdot 10^4$ nT and $m=2.71$, and selected the values of B_0 , L and α to fit the CAN model at $5 R_J$, where $B=3144$ nT according to CAN model. They chose: $B_0=3.335 \cdot 10^5$ nT, $L=14.5 R_J$ and $\alpha=5/2$. As shown later, these parameters need to be modified to better fit the Galileo observations. Using (3) and (9), an expression of the flux function is obtained:

$$F_e(\rho_e) = F_\infty + \frac{B_0 R_J^3}{\alpha L} \Gamma \left[-\alpha, \left(\frac{\rho_e}{L} \right)^\alpha \right] + \frac{A}{m-2} \left(\frac{R_J}{\rho_e} \right)^{m-2}. \quad (11)$$

$\Gamma(a, z)$ is the incomplete gamma function: $\Gamma[a, z] = \int_z^\infty t^{a-1} e^{-t} dt$. The constant F_∞ is obtained by adjusting F_e to the CAN model value in the inner magnetosphere. We use $F_e = 8.82 \cdot 10^4$ nT R_J^2 at $5 R_J$.

In general, the angular velocity can be calculated by a numerical integration of (9), considering (10), (11) and assuming exact plasma corotation in the vicinity of the Io torus ($\omega=\Omega$

for $\rho_e \sim 5\text{-}10 R_J$, typically). As shown by *Nichols and Cowley*, [2004], useful approximations to the angular velocity can also be computed considering the simple power law expression of B_{ze} (the ‘KK’ model) and assuming that $F_e(\rho)$ is a constant (F_0) representative of the value of F_e in the plasma-disc.

With $B_{ze}(\rho_e) = -A \left(\frac{R_J}{\rho_e}\right)^m$, equation (8) becomes

$$\frac{1}{\rho_e} \frac{d}{d\rho_e} \left(\rho_e^2 \frac{\omega}{\Omega} \right) = 4 \left(\frac{R_H}{\rho_e} \right)^m \left(1 - \frac{\omega}{\Omega} \right), \quad (12)$$

where R_H is a typical length (the Hill radius) that scales the decreasing angular speed with radial distance:

$$R_H = \left(\frac{2\pi\Sigma F_0 A}{\dot{M}} \right)^{1/m}. \quad (13)$$

The solution of (8) can then be written:

$$\frac{\omega}{\Omega} = \left(\frac{4}{m} \right)^{2/m} \left(\frac{R_H}{\rho_e} \right)^2 \exp \left[\frac{4}{m} \left(\frac{R_H}{\rho_e} \right)^m \right] \times \left[\Gamma \left[1 - \frac{2}{m}, \frac{4}{m} \left(\frac{R_H}{\rho_e} \right)^m \right] + K \right] \quad (14)$$

where K is an integration constant determined by imposing the condition of exact corotation at a specified distance from Jupiter.

It is interesting to note that the numerical solution of equation (9) as the approximate solution (14) only weakly depends on this boundary condition. In practice, one can impose the condition $\omega\Omega=1$ at different ρ_e (in the range 5-15 R_J for example) without significantly modifying the function $\omega(\rho)\Omega$. From expression (14), one can indeed check that the solutions obtained by fixing $\omega\Omega=1$ at different ρ_e merge with the $K=0$ solution over a short distance. This simplifies

the analysis since Σ/\dot{M} and B_{ze} are then sufficient to determine the $\omega\Omega$ profile. $B_\phi(\rho)$ is then obtained by combining (6) and (14), or alternatively (6) and the numerical solution of (9).

Having obtained B_z and then F_e from observations, and setting Σ to a constant value, here taken to be 1 S, $B_\phi(\rho)$ appears to be a function of the ratio Σ/\dot{M} . This function of Σ/\dot{M} can be called the ‘ B_ϕ profile’ and characterizes the way B_ϕ varies with the radial distance. In practice, it can be obtained by combining (6) and (14). As shown in the next section, the B_ϕ profile significantly changes with Σ/\dot{M} . It is thus interesting to compare the profiles with the observations of B_ϕ to identify values of Σ/\dot{M} and Σ that offer good fits. This will be used to estimate the outflows corresponding to regimes of low and high magnetospheric activity.

3.2- APPLICATION

We first determine the function F_e that establishes the magnetic mapping between the ionosphere and the magnetosphere. We thus use equation (10) and fit the measured B_z by modifying the values of B_0 , L , α , A and m . As noticed by *Kivelson and Khurana* [1993], the measurement of B_z is not straightforward: close to the current sheet center any variations in the normal-to-the-disc orientation lead to errors in the determination of the normal magnetic field. We thus follow their method and determine the minimal value of B at each crossing of the current sheet center, considering that this minimum is a good approximation to the actual B_z . These measurements are shown in Figure 8, for the three orbits discussed previously as well as for the period DOY 251-265, 1996, another interesting radial pass through the magnetodisc.

The fits are performed by first considering the region beyond $30 R_J$ which is used to determine the power law term in equation (10) (A and m). The complete fit is then obtained by adjusting L in the first term of (10). Using Voyager data, on the dayside, *Nichols and Cowley* [2004] get $L=14.5 R_J$. The best fits of Galileo measurements, on the nightside, give larger L ($L\sim 17-19 R_J$). The two additional parameters (B_0 and α) are then determined by imposing continuity with the internal field ($B=3144$ nT at $5 R_J$ according to CAN model) and the ‘disc’

field (from A and m). These fits are shown in the plots, together with the dipole values and Nichol's determinations. In general, we get flatter profiles in the disc than Nichol's determinations, with values of m varying between -1.2 and -1.7, instead of -2.7. The magnetic flux function is then computed from (11) (lowest panel in Figure 9).

The angular velocity can be obtained either by solving (9) or using (14). We verify that the results obtained by the two methods differ little (less than 10%). For practical reasons we apply formula (14), choosing $F_0 = F_e(60 R_J)$. The angular velocity is then determined for various values of the ratio $SM = \Sigma / \dot{M}$, with the boundary condition ($\omega = \Omega$) imposed at $\rho_e = 10 R_J$. We consider values of the parameter SM varying from 0.1 to 0.8 (where Σ is expressed in S and \dot{M} in tons/s). The rotation profiles are shown as normalized angular velocity (ω / Ω) vs. radial distance in the equator in Figure 9. The canonical value is $SM = 0.1$, corresponding to $\Sigma = 0.1$ S and $\dot{M} = 1$ tons/s. However, Σ may be larger since the parallel current and the electron precipitation enhance the Pedersen conductivity [Nichols *et al.*, 2005, Ray *et al.*, 2010] and \dot{M} may be smaller than 1 tons/s (see estimates in Bagenal and Delamere, [2010]), so that $SM = 0.1$ is likely a rather low value.

As seen in Figure 8, beyond $\sim 40 R_J$, the profiles decrease almost linearly with distance, by 10 to 20 % from 40 to 80 R_J , with values at 40 R_J that strongly vary with SM , from ~ 0.55 ($SM = 0.1$) to ~ 0.9 ($SM = 0.8$). Inside 40 R_J , the profiles vary from one orbit to the other, with a more or less rapid lag from corotation as the distance increases.

These differences are important for determining the B_ϕ profile. Equation (6) shows that B_ϕ is proportional to the lag from corotation and the Pedersen conductivity. Close to corotation and for a given conductivity, even small variations of ω have important effects on B_ϕ . This implies that the profile of B_ϕ varies strongly with the parameter SM . This is shown in the left panels of Figure 10 where B_ϕ is plotted as a function of the radial distance, for the different orbits and SM varying from 0.1 to 0.8. These profiles are computed assuming $\Sigma = 1$ and \dot{M} chosen to match the values of SM .

These profiles are compared with the measured B_ϕ in the right panels of Figure 10. The measured values of B_ϕ are identical to those used in section 2.3. As for Figure 5, they correspond to measurements performed between two successive crossings of the center of the current sheet, at each incursion of Galileo into the lobes or, close to Jupiter (distance $< 25 R_J$), when Galileo is at maximum distance from the sheet.

Formally, the comparison between the measured and the model B_ϕ cannot give independently Σ and \dot{M} (or Σ and SM). One parameter needs to be selected (SM for example), before the other (Σ) can be deduced from the measurements. As discussed previously, selecting SM leads to imposing the shape of the radial profile of B_ϕ , with a remaining degree of liberty corresponding to a multiplicative constant (Σ in practice). One can try to select profiles that provide apparent good fits to B_ϕ and selecting a value of the Pedersen conductivity to match the measurements. Generally, the fit cannot be done with a single choice of Σ and \dot{M} since we have chosen examples that present an important time variability, in particular due to the events. These events correspond to the B_ϕ peaks seen in the middle of the magnetosphere. The principle is thus rather to determine a couple Σ and \dot{M} that may explain the lower values of B_ϕ - they would be representative of the ‘quiet’ magnetosphere – and another couple for the largest values that would characterized the ‘active’ magnetosphere.

The small values of B_ϕ ($B_\phi < 1$ nT) are the easiest to interpret. The smallest B_ϕ curves are obtained for the larger values of SM (0.7-0.8). If Pedersen conductance is taken at the canonical value of 0.1 S, good fits are then obtained for a mass outflow of ~ 125 -140 kg/s. The corresponding curves are shown in orange in Figure 9. Fits corresponding to smaller SM ($SM=0.1$ -0.2) would require smaller Σ ($\Sigma < 0.05$) and, consequently, much larger mass outflows: $\dot{M} = \Sigma/SM > 2$ tons/s. The choice $\Sigma=0.1$ S and $\dot{M} \sim 120$ -150 kg/s is then likely more representative.

The fit of the maximal B_ϕ ($B_\phi > 5$ nT) is more ambiguous. Values of 5-6 nT are observed at 40-50 R_J and above 7 nT below 30 R_J . One possibility is to again consider large SM profiles. As

seen in the plots, this requires a Pedersen conductivity close to 1 S ($\Sigma=1.2-1.5$ for $SM=0.7-0.8$), with a mass outflow of 1.2-1.8 tons/s. This corresponds to the red curves in Figure 8. Nevertheless, the use of small SM profiles is also possible. With $SM=0.2$ and $\Sigma \sim 0.5$, for example, one obtains $B_\phi \sim 6-8$ nT. The required mass outflow would then be higher, in the range $\sim 2.5-3$ tons/s (profiles in blue). Without independent determinations of Σ or \dot{M} , these two options cannot be excluded for explaining the large B_ϕ . In principle, with a sufficient number of measurements, it could have been possible to select the model profile (the red or the blue curves in the plot) that best fits the observations. The profiles indeed significantly differ for radial distance smaller than $\sim 30 R_J$, unfortunately there are too few measurements in that radial range to identify the best profile. Nevertheless, despite this ambiguity, the key result is that the application of Hill's model shows that the difference between the low and the large twist situations (small/large B_ϕ) can be explained by increases of the mass outflow by factors of 10 to 20, from 100-200 kg/s to 1.5-3 tons/s, typically.

The first conclusion of this study is that the prediction of B_ϕ from Hill's model are consistent with the observations, using ranges for the Pedersen conductivity and the mass outflow rate that are close to the canonical values. A similar result was obtained by Cowley *et al*, [2008], with the demonstration that a representative angular velocity profile leads to B_ϕ profiles that compare favorably with the data. The new point presented here concerns the temporal variations of this system, with the conclusion that the variations of the radio intensity, that are correlated with those of B_ϕ , can be explained by modulations of the mass flow rates from 100-200 kg/s to 2 tons/s, from quiet to active periods.

4-Discussion and conclusions

It is interesting to consider the observations and the model to estimate some important terms in the power budget of the Jovian system. The power dissipated in the plasma-disc by the torque of

the current system is $\delta W_D = \rho_e i_\rho B_{ze} \omega$ (per surface unit). Integrated in azimuth, one gets the power dissipated per radial unit length:

$$\delta W_D = 8\pi\Omega^2\Sigma\rho_e F_e |B_{ze}| \left(1 - \frac{\omega}{\Omega}\right) \frac{\omega}{\Omega}. \quad (15)$$

and, integrated over the whole disc, the total dissipated power is:

$$\delta W_D = 8\pi\Omega^2\Sigma \int_{\rho_0}^{\rho_1} \rho_e F_e |B_{ze}| \left(1 - \frac{\omega}{\Omega}\right) \frac{\omega}{\Omega} d\rho_e. \quad (16)$$

Using this expression with $\rho_0 = 10 R_J$ and $\rho_1 = 80 R_J$, we get a power dissipation of $1.05 \cdot 10^{14}$ to $1.8 \cdot 10^{14}$ W (depending on the orbit) for quiet situations, i.e. when B_ϕ is close to the model values, with $\Sigma=0.1$, $SM=0.7$ and mass outflow of ~ 125 - 140 kg/s. According to (16), the power dissipation would increase by a factor of 10 in the case of strong activity, with $B_\phi \sim 5$ - 6 nT. In this case one gets values ranging from $0.96 \cdot 10^{15}$ to $1.6 \cdot 10^{15}$ W, which is slightly higher than the estimates given by *Cowley et al*, [2005]. These estimates do not significantly change with the choice of SM , with less than 5% of differences between the low SM ($SM=0.2$, $\Sigma \sim 0.5$ and $\dot{M} \sim 2.5$ - 3 t/s) and the large SM possibility ($SM=0.7$, $\Sigma \sim 1.2$ - 1.5 and $\dot{M} \sim 1.2$ - 1.6 t/s).

To compare this power with the radiated power flux, aI and mI need to be converted into radiated power. This cannot be done very accurately since the radio emission cones are not known with certainty. Nevertheless, if one assumes that the radio waves are emitted in a $\frac{1}{2}$ space and knowing that the HOM flux is about half the total radio flux (see plots in *Zarka*, [1998]), the radio power would be related to the radio intensity, normalized to $10 R_J$, by: P_{rad} (in W) $\sim 2 \cdot 10^{16} aI$ (or mI). Considering the averaged radio power, this gives $P_{rad} \sim 3 \cdot 10^8$ W for the quiet magnetosphere, when the disc magnetic twist is close to the model values, and $P_{rad} \sim 2 \cdot 10^9$ W in case of strong activity, when the twist doubles compared to its model value. The global

conversion factor is thus about 10^{-6} , from the power dissipated in the disc by the torque exerted by the M-I coupling current system to the resulting radiated radio power.

In summary, the general model of jovian magnetospheric activity sketched in Figure 1 appears to be remarkably consistent with the Galileo observations. Episodes of large bend-back B_ϕ in the magnetodisc (5-6 nT, meaning 2-3 times the values given by Khurana's model), thus of large magnetic twist, are well correlated with periods of strong radio fluxes. As this is observed both in the post and pre mid-night sector with systematically B_ϕ variations in the bend-back direction, this supports the hypothesis of the dominant role of the internal processes. The large B_ϕ result from large radial currents flowing in the disc and thus indicate an enhanced M-I coupling system and strong parallel currents, with most certainly larger parallel electric fields, stronger particle acceleration in the auroral zone, and, consistent with the current knowledge of the cyclotron maser mechanism, the generation of more powerful radio emission. The Juno mission will certainly help to document and clarify this chain of auroral processes.

The analysis also confirms the very consistent picture offered by Hill's model. The observed values of B_ϕ are easily explained by the model assuming values of the Pedersen conductivity and the outward mass flux that are in the range of the canonical values, from 0.1 to 1.5 S and 120-150 kg/s to ~ 2 tons/s. The activity of the jovian system would thus be regulated by variations of the outward mass flow rate in the disc, with peaks of activity corresponding to the 'energetic events' described by *Louarn et al.*, [1998]. Our hypothesis is that the origin of this key process is internal to the jovian magnetosphere, possibly in the outer region of the Io torus ($\sim 8-12 R_J$) where energetic particle injections are observed [*Mauk et al.*, 1999, 2002; *Louarn et al.*, 2001, 2014].

The origin of this internal process is unlikely associated to variations in the plasma production rate. The physical/chemical processes involved in Io's plasma production are indeed far too slow to explain variations of \dot{M} at day scales; they are rather expected to operate at month scales in case of variations of the volcanic activity [*Delamere et al.*, 2004, *Steffl et al.*, 2007]. A more likely hypothesis is the existence of a global instability, starting typically at $8-12 R_J$, where the injections are observed. This internal instability would lead to sudden variations in the mass

outflow from the outer Io torus to the inner disc, with variation of \dot{M} at day scales due to more efficient radial transport processes. The relevant mechanism should associate inward energetic particles injections and outward cold/thermal plasma transports. Physically, the permanent plasma production could lead to a progressive approach of marginal stability in outer torus/inner disc so that the system becomes easy to destabilize either by self or externally-driven triggers. This inner mechanism could in certain circumstances be externally triggered, which may explain why the Jovian activity is also related to solar wind perturbations.

Acknowledgment: We thank the Centre de Données de la Physique des Plasma (CDPP) for the use of AMDA, the automated data selection software developed at CDPP. On the French side, this work has been permitted by the support of CNES and CNRS.

References

- Bagenal, F., and J.D. Sullivan (1981), Direct plasma measurements in the Io torus and inner magnetosphere of Jupiter, *J. Geophys. Res.*, 86, 8447-8466, doi: 10.1029/JA096iA10p08447.
- Bagenal, F., and P. ~~A2010JA016294~~ (2010), Review of mass and energy in the magnetospheres of Jupiter and Saturn, *J. Geophys. Res.*, 116, A05209, doi:10.1029/2010JA016294.
- Belcher, J.W., (1983), The low-energy plasma in the jovian magnetosphere, in *Physics of the Jovian Magnetosphere*, edited by A.J. Dessler, pp. 68-105, Cambridge University Press, Cambridge, UK, doi:10.1029/CBO9780511564574.005
- Chiu, Y.T., and M. Schulz (1978), Self-consistent particle and parallel electrostatic field distributions in the magnetospheric-ionospheric auroral region, *J. Geophys. Res.*, 83, 629
- Clarke, J. T., D. Grodent, S. W. H. Cowley, E. J. Bunce, P. M. Zarka, J. E. P. Connerney, and T. Satoh (2004), Jupiter's aurora, in *Jupiter: The Planet, Satellites and Magnetosphere*, edited by F. ~~Bagenal~~ B. ~~McKinnon~~, Cambridge Univ. Press, Cambridge, U. K.
- Connerney, J. E. P.; Acuna, M. H. and Ness, N. F.(1981), Modeling the Jovian current sheet and inner magnetosphere, *J. Geophys. Res.*, vol. 86, p. 8370-8384, doi: 10.1029/JA086iA10p08370
- Cowley, S. W. H., and E. J. Bunce (2001), Origin of the main auroral oval in Jupiter's coupled magnetosphere-ionosphere system, *Planet. Space Sci.*, 49, 1067–1088.
- Cowley, S. W. H., J. D. Nichols, and E. J. Bunce (2002), Distributions of current and auroral precipitation in Jupiter's middle magnetosphere computed from steady-state Hill-Pontius angular velocity profiles: Solutions for current sheet and dipole magnetic field models, *Planet. Space Sci.*, 50, 717–734.

- Delamere, P. A., A. Steffl, and F. Bagenal (2004), Modeling temporal variability of plasma conditions in the Io torus during the Cassini era, *J. Geophys. Res.*, 109, 10,216, doi:10.1029/2003JA010354
- Delamere, P. A., A. Otto, X. Ma, F. Bagenal, and R. J. Wilson,(2015 a) Magnetic flux circulation in the rotationally-driven giant magnetospheres, *J. Geophys. Res.*, doi:10.1002/2015JA021036, 2015JA021036
- Delamere, P. A., F. Bagenal, C. Paranicas, A. Masters, A. Radioti, B. Bonfond, L. Ray, X. Jia, J. Nichols, and C. Arridge, (2015 b) Solar Wind and Internally Driven Dynamics: Influences on Magnetodiscs and Auroral Responses, *Space Science Reviews*, 187, 51-97, doi10.1007/s11214-014-0075
- Delory, G. T., R. E. Ergun, C. W. Carlson, L. Muschietti, C. C. Chaston, W. Peria, and J. P. McFadden (1998), FAST observations of electron distributions within AKR source, *Geophys. Res. Lett.*, 25, 2069–2072, doi:10.1029/98GL00705.
- Ergun, R. E., *et al.* (1998), FAST satellite wave observations in the AKR source region, *Geophys. Res. Lett.* 25, 2061–2064.
- Ergun, R. E., C. W. Carlson, J. P. McFadden, F. S. Mozer, and R. J. Strangeway (2000a), Parallel electric fields in discrete arcs, *Geophys. Res. Lett.*, 27, 4053–4056, doi:10.1029/2000GL003819.
- Ergun, R. E., C. W. Carlson, J. P. McFadden, G. T. Delory, R. J. Strangeway, and P. L. Pritchett (2000b), Electron-cyclotron maser driven by charged-particle acceleration from magnetic field-aligned electric fields, *Astrophys. J.*, 538, 456–466.
- Ergun, R. E., L. Ray, P. A. Delamere, F. Bagenal, V. Dols, and Y. Su (2009), Generation of parallel electric fields in the Jupiter-Io torus wake region, *J. Geophys. Res.*, 114, A05201, doi:10.1029/2008JA013968.
- Evans, D.S., Precipitation electron fluxes formed by a magnetic field-aligned potential difference, *J. Geophys. Res.*, 79, 2853,1974

- Ge, Y.S., Jian, L.K. and C. T. Russell, (2007), Growth phase of jovian substorms, *Geophys. Res. Lett.*, *34*, L23106, doi:10.1029/2007GL031987
- Genova, F., P. Zarka, and C.H. Barrow (1987), Voyager and Nancay observations of the Jovian radio-emission at different frequencies—solar wind effect and source extent, *Astron. Astrophys.*, *182* (1987), pp. 159–162
- Grodent, D., J. T. Clarke, J. Kim, J. H. Waite Jr., and S. W. H. Cowley (2003), Jupiter's main auroral oval observed with HST-STIS, *J. Geophys. Res.*, *108* (A11), 1389, doi:10.1029/2003JA009921.
- Gurnett, D.A., (1974), The Earth as a radio source: Terrestrial kilometric radiation, *J. Geophys. Res.*, *79*, 4227.
- Gurnett, D.A., W.S. Kurth, R.R. Shaw, A.Roux, R.Gendrin, C.F.Kennel, F.L. Scarf, and S.D. Shawhan, (1992), The Galileo plasma waves investigation, *Space Sci. Rev.*, *60*, 341.
- Gurnett, D.A., W. S. Kurth, G. B. Hospodarsky, A. M. Persoon, P. Zarka, A. Lecacheux, S. J. Bolton, M. D. Desch, W. M. Farrell, M. L. Kaiser, H.-P. Ladreiter, H. O. Rucker, P. Galopeau, P. Louarn, D. T. Young, W. R. Pryor, and M. K. Dougherty, (2002) Control of Jupiter's Radio Emission and Aurorae by the Solar Wind, *Nature*, *415*, 985-987.
- Hess, S. L. G., E. Echer, P. Zarka, L. Lamy, and P. A. Delamere, (2014) Multi-instrument study of the Jovian radio emissions triggered by solar wind shocks and inferred magnetospheric subcoangular velocitys, *Planet. Space Sci.*, *99*, 136-148, doi10.1016/j.pss.2014.05.015.
- Hill, T. W., (1979), Inertial limit on corotation, *J. Geophys. Res.*, *84*, 6554–6558, doi:10.1029/JA084iA11p06554.
- Hill, T. W. (2001), The Jovian auroral oval, *J. Geophys. Res.*, *106* (A5), 8101–8108, doi:10.1029/2000JA000302.

- Hill, T. W., A. J. Dessler, and C. K. Goertz, (1983), Magnetospheric models, in *Physics of the Jovian Magnetosphere*, edited by A.J. Dessler, pp. 353-394, Cambridge University Press, Cambridge, UK, doi:10.1029/CBO9780511564574.005.
- Khurana, K. K., and M. G. Kivelson (1993), Inference of the angular velocity of plasma in the Jovian magnetosphere from the sweepback of magnetic field, *J. Geophys. Res.*, 98(A1), 67–79, doi:10.1029/92JA01890.
- Khurana, K. K., Kivelson, M. G., Vasyliunas, V. M., Krupp, N., Woch, J., Lagg, A., Mauk, B. H., Kurth, W. S., (2004), The configuration of Jupiter's magnetosphere, in *Jupiter: The Planet, Satellites, and Magnetosphere*, edited by F. Bagenal, T. E. Dowling, and W. B. McKinnon, pp. 593–616, Cambridge Univ. Press, Cambridge, U. K.
- Kivelson, M. G., K. K. Khurana, J. D. Means, C. T. Russell, and R. C. Snare (1992), The Galileo magnetic field investigation, *Space Sci. Rev.*, 60, 357-383.
- Knight, S. (1973), Parallel electric fields, *Planet. Space Sci.*, 21, 741–750
- Krimigis, S. M., and E.C. Roelof, (1983), Low energy particle population, in *Physics of the Jovian Magnetosphere*, edited by A.J. Dessler, pp. 106-156, Cambridge University Press, Cambridge, UK, doi:10.1029/CBO9780511564574.005
- Krupp, N., *et al.* (2004b), Dynamics of the Jovian magnetosphere, in *Jupiter: The Planet, Satellites, and Magnetosphere*, edited by F. Bagenal, T. E. Dowling, and W. B. McKinnon, pp. 617–638, Cambridge Univ. Press, Cambridge, U. K.
- Kurth, W. S., and D. A. Gurnett (1998), Auroral kilometric radiation integrated power flux as a proxy for A_E , *Adv. Space Res.*, 22, 73–77.
- Kurth W. S. et al., (2005) An Earth-Like Correspondence Between Saturn's Auroral Features and Radio Emission, *Nature*, 433, 722-725
- L. Lamy, R. Prange, W. Pryor, J. Gustin, S. V. Badman, H. Melin, T. Stallard, D. G. Mitchell, and P. C. Brandt, Multispectral Simultaneous Diagnosis of Saturn's Aurorae Throughout a

Planetary Rotation, *J. Geophys. Res.*, *118*, pp. 4817-4843, doi:10.1002/jgra.50404, August 1, 2013.

Louarn, P., C. P. Paranicas, and W. S. Kurth (2014), Global magnetodisc disturbances and energetic particle injections at Jupiter, *J. Geophys. Res.*, *119*, 4495–4511, doi:10.1002/2014JA019846.

Louarn, P., Roux, A., Perraut, S., Kurth, W. and D. A. Gurnett, (1998), A study of the largescale dynamics of the jovian magnetosphere using the Galileo plasma wave experiment, *Geophys. Res. Lett.*, *25*, 2905–2908.

Louarn, P., A. Roux, H.de Féraudy, D. Le Quéau, M.André and L. Matson, (1990) Trapped electrons as a free sources for the auroral kilometric radiation, *J. Geophys. Res.*, *96*, 5983

Louarn, P., Roux, A., Perraut, S., Kurth, W. S. and D. A. Gurnett, (2000), A study of the Jovian “energetic magnetospheric events” observed by Galileo: role in the radial plasma transport, *J. Geophys. Res.*, *105*, 13 073–13 088.

Louarn P., B. Mauk, D. J. Williams, C. Zimmer, M.G. Kivelson, W.S. Kurth, D.A. Gurnett and A. Roux, (2001), A multi-instrument study of a jovian magnetospheric disturbance, *J. Geophys. Res.*, *106*, 29883.

Lyons, L. R. (1980), Generation of large-scale regions of auroral currents, electric potentials, and precipitation by the divergence of the convection electric field, *J. Geophys. Res.*, *85(A1)*, 17–24, doi:10.1029/JA085iA01p00017

McFadden, J. P., C. W. Carlson, and R. E. Ergun (1999), Microstructure of the auroral acceleration region as observed by FAST, *J. Geophys. Res.*, *104(A7)*, 14453–14480, doi:10.1029/1998JA900167.

Mauk, B.H., D.J. Williams, R.W. McEntire , K.K. Khurana, and J. D. Roederer, (1999), Storm-like dynamics of Jupiter’s inner magnetosphere, *J. Geophys. Res.*, *104*, 22759.

- Mauk, B. H., J. T. Clarke, D. Grodent, J. H. Waite Jr., C. P. Paranicas, and D. J. Williams (2002), Transient aurora at Jupiter from injections of magnetospheric electrons, *Nature*, 415, 1003.
- Nichols, J. D. (2011), Magnetosphere-ionosphere coupling in Jupiter's middle magnetosphere: Computations including a self-consistent current sheet magnetic field model, *J. Geophys. Res.*, 116, A10232, doi:10.1029/2011ja016922.
- Nichols, J. D., and S. W. H. Cowley (2003), Magnetosphere-ionosphere coupling currents in Jupiter's middle magnetosphere: Dependence on the effective ionospheric Pedersen conductivity and iogenic plasma mass outflow rate, *Ann. Geophys.*, 21, 1419–1441.
- Nichols, J. D., and S. W. H. Cowley (2004), Magnetosphere-ionosphere coupling currents in Jupiter's middle magnetosphere: Effect of precipitation-induced enhancement of the ionospheric Pedersen conductivity, *Ann. Geophys.*, 22, 1799–1827.
- Nichols, J. D., and S. W. H. Cowley (2005), Magnetosphere-ionosphere coupling currents in Jupiter's middle magnetosphere: Effect of magnetosphere-ionosphere decoupling by field-aligned auroral voltages, *Ann. Geophys.*, 23, 799–808.
- Nichols, J. D., J. T. Clarke, J.-C. Gérard, D. Grodent, and K. C. Hansen (2009), Variation of different components of Jupiter's auroral emission, *J. Geophys. Res.*, 114, A06210, doi:10.1029/2009JA014051.
- Nichols, J. D., N. Achilleos, and S. W. H. Cowley (2015), A model of force balance in Jupiter's magnetodisc including hot plasma pressure anisotropy, *J. Geophys. Res. Space Physics*, 120, 10,185–10,206, doi:10.1002/2015JA021807.
- Pontius, D. H., Jr. (1997), Radial mass transport and rotational dynamics, *J. Geophys. Res.*, 102(A4), 7137–7150, doi:10.1029/97JA00289.
- Prangé, R., L. Pallier, K.C. Hansen, R. Howard, A. Vourlidas, R. Courtin, and C. Parkinson,(2004), An interplanetary shock traced by planetary auroral storms from the Sun to Saturn, *Nature*, 432, pp. 78–81.

- Ray, L. C., Y. Su, R. E. Ergun, P. A. Delamere, and F. Bagenal (2009), Current-voltage relation of a centrifugally confined plasma, *J. Geophys. Res.*, *114*, A04214, doi:10.1029/2008JA013969
- Ray, L. C., R. E. Ergun, P. A. Delamere, and F. Bagenal (2010), Magnetosphere-ionosphere coupling at Jupiter: Effect of field-aligned potentials on angular momentum transport, *J. Geophys. Res.*, *115*, A09211, doi:10.1029/2010JA015423.
- Ray, L. C., N. A. Achilleos, and J. N. Yates (2015), The effect of including field-aligned potentials in the coupling between Jupiter's thermosphere, ionosphere, and magnetosphere, *J. Geophys. Res. Space Physics*, *120*, 6987–7005, doi:10.1002/2015JA021319.
- Reiner, M. J., J. Fainberg, R. G. Stone, M. L. Kaiser, M. D. Desch, R. Manning, P. Zarka, and B.-M. Pedersen (1993), Source characteristics of Jovian narrow-band kilometric radio emissions, *J. Geophys. Res.*, *98*(E7), 13163–13176, doi:10.1029/93JE00536.
- Roux, A., A. Hilgers, H. deFeraudy, D. le Queau, P. Louarn, S. Perraut, A. Bahnsen, M. Jespersen, E. Ungstrup, and M. Andre (1993), Auroral kilometric radiation sources: In situ and remote observations from Viking, *J. Geophys. Res.*, *98*(A7), 11657–11670, doi:10.1029/92JA02309.
- Steffl, A. J., F. Bagenal, and P. A. Delamere (2008), Cassini UVIS observations of the Io plasma torus: IV. Modeling temporal and azimuthal variability, *Icarus*, *194*, 153–165, doi:10.1016/j.icarus.2007.09.016
- Vasyliunas, V. M., (1983), Plasma distribution and flow, in *Physics of the Jovian Magnetosphere*, edited by A.J. Dessler, pp. 395–453, Cambridge University Press, Cambridge, UK, doi:10.1029/CBO9780511564574.005
- Zarka, P., (1998), Auroral radio emissions at the outer planets: Observations and theories, *J. Geophys. Res.*, *10* (E9), 20159–20194.

Figure Captions:

Figure 1: Sketch of Jovian magnetospheric activity, with the global configuration of the M-I coupling current system showing field lines and associated auroral processes in a meridian plane near the ionosphere (top left) and in a full cut from north to south (top right). The magnetic configuration and local currents are sketched in a 3-D element of the magnetodisc (lower right).

Figure 2. PWS and MAG observations from DOY 77 to 92, 1997. Panel (a): Spectral intensity measured by PWS from ~50 kHz to 5.6 MHz (electric component). Panel (b): Spectral intensity measured by PWS from 5 Hz to 10 kHz. Panel (c): ‘HOM’ intensity from 300 kHz to 5.6 MHz (in black: averaged over a sliding 1-hour window, in blue: maximum over a jovian rotation, in red: averaged over a jovian rotation). Panel (d) and (e): absolute values of the radial (B_r) and the azimuthal (B_ϕ) magnetic components (SYS3 coordinates); in black: MAG measurements, in red: Khurana’s model field, in blue (panel d) total field. Panel (e) and panel (f): magnetic bending angle: $\zeta = \text{atan}(B_\phi/B_r)$ and normalized twist: ($Tw=B_\phi/rB_r$ in R_J^{-1}). In blue: measured values, shown as black bars: their averaged values measured between two sheet crossings, in red: the model values averaged over the same interval.

Figure 3. PWS and MAG observations from DOY 166 to 176, 1997 and DOY 251 to 259, 1997. The same quantities as in Figure 2 are displayed, with the same color code: Panel (a): ‘HOM’ intensity from 300 kHz to 5.6 MHz; Panel (b) and (c): absolute values of the radial (B_r) and the azimuthal (B_ϕ) magnetic components (SYS3 coordinates); Panel (d) and panel (e): magnetic bending angle: $\zeta = \text{atan}(B_\phi/B_r)$ and normalized twist: ($Tw=B_\phi/r.B_r$ in R_J^{-1}). The abscissa is the Galileo/Jupiter distance. The dates are given in the upper part of each plot.

Figure 4. Plot of the radio intensity as a function of the difference between the measured twist (in R_J^{-1}) and the model values. On the left, the maximal intensity is plotted, on the right, the averaged intensity. The lowermost plots display all three orbits. The green lines are linear fits.

Figure 5. Plot of the averaged radio intensity as a function of the difference between the measured B_ϕ and the model values. On the left, the intensity is plotted vs. difference in nT between the averaged B_ϕ and the model, on the right, the difference in nT between the maximum B_ϕ and the model. The normalized chi-squared value of the linear fit (in green) is indicated in each plot.

Figure 6. On the left, plot of the averaged radio intensity as a function of the difference in nT between the measured total B and the model values (B_{red}). On the right, plot of the averaged radio intensity as a function of the difference in nT between the measured radial B component and the model values (B_{tot}). The normalized chi-squared value of the linear fit (in green) is indicated in each plot.

Figure 7. PWS and MAG observations from DOY 178 to 188, 1997. The same quantities as in Figure 2 are displayed, with the same color code: Panel (a); spectral intensity; panel (b): ‘HOM’ intensity from 300 kHz to 5.6 MHz; Panel (c) and (d): radial (B_r) and the azimuthal (B_ϕ) magnetic components (SYS3 coordinates); Panel (e): magnetic bending angle: $\zeta = \text{atan}(B_\phi/B_r)$, calculated from a 3 hour averaging. Negative angles correspond to bend-back tilt. Panel (f): range and LT.

Figure 8. The first four panels show the measured B_z component at the center of the current sheet and fits with equation (10) (solid lines of different colors for different orbits). The dashed blue lines are the dipole field, and the dashed black lines are Nichols’s fits. The lowermost plot shows the fitted magnetic flux function for the different orbits with the same color coding. Again in this panel, the dashed curve is from the *Nichols and Cowley* [2004] model.

Figure 9. Profiles of the normalized angular velocity (ω/Ω), for the different orbits plotted in Figure 6 and for values of the parameter $SM=\Sigma/\dot{M}$ varying from 0.1 to 0.8. The lowermost plot corresponds to the angular velocitys computed using averaged coefficients for the magnetic fit (averaged magnetic flux function).

Figure 10. Plots on the left: profiles of B_ϕ , for the different orbits and SM varying from 0.1 to 0.8. The profiles are computed assuming $\Sigma=1$ and \dot{M} chosen to match the values of SM . Plots on the right: comparison between the model and measurements (black stars). The low B_ϕ are fitted with $\Sigma=0.1$ and $SM=0.7$ or 0.8 ; thus with a mass outflow rate of ~ 125 - 140 kg/s (orange curves). The large B_ϕ are fitted with $\Sigma=1.2$ - 1.5 and $SM=0.7$ - 0.8 , with a mass outflow rate of 1.2 - 1.8 t/s (red curves) or, alternatively, with $\Sigma \sim 0.5$ and $SM=0.2$, with a mass outflow rate of 2.5 - 3 t/s (blue curves).

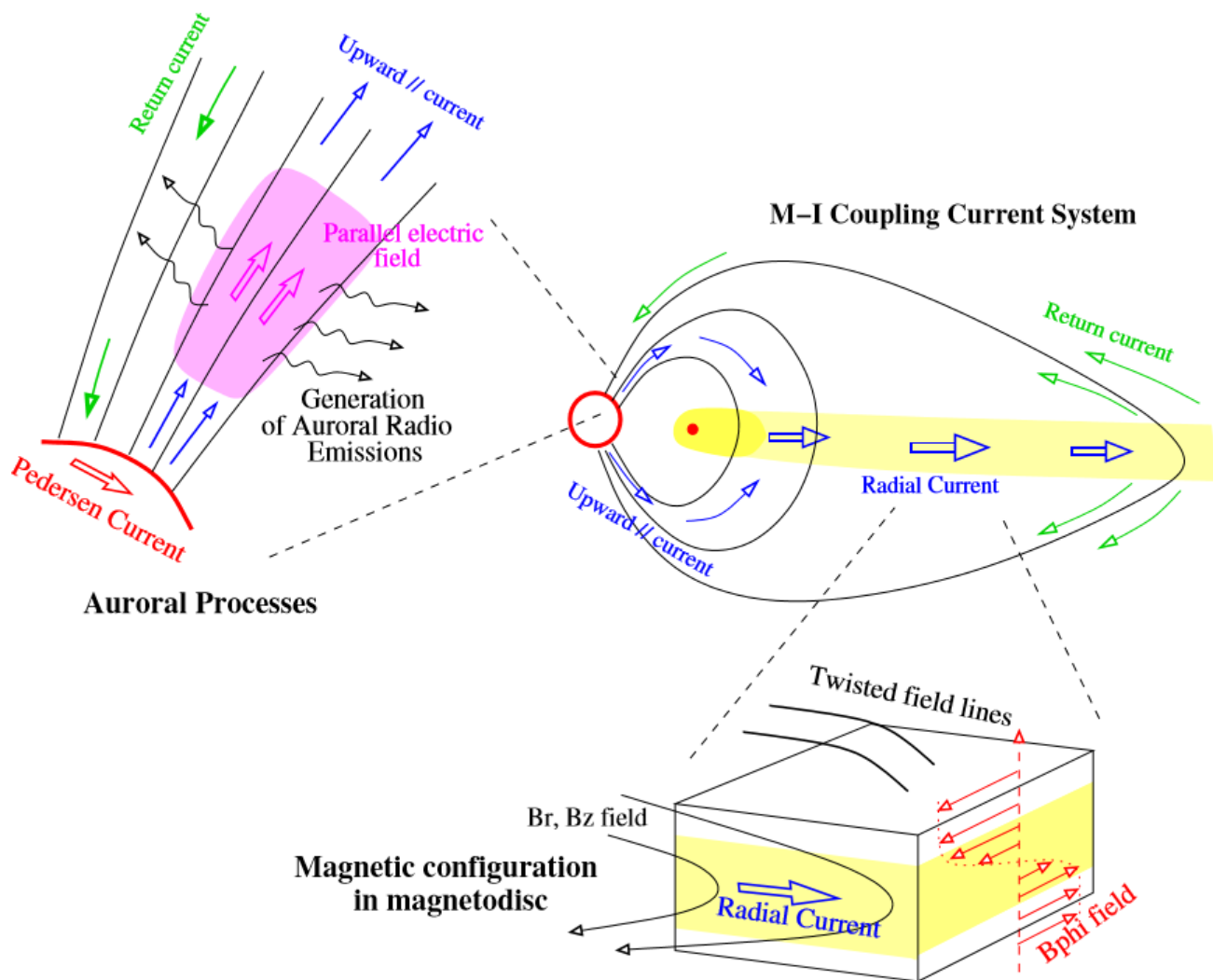


Figure 1: Sketch of Jovian magnetospheric activity, with the global configuration of the M-I coupling current system showing field lines and associated auroral processes in a meridian plane near the ionosphere (top left) and in a full cut from north to south (top right). The magnetic configuration and local currents are sketched in a 3-D element of the magnetodisc (lower right).

Figure 2

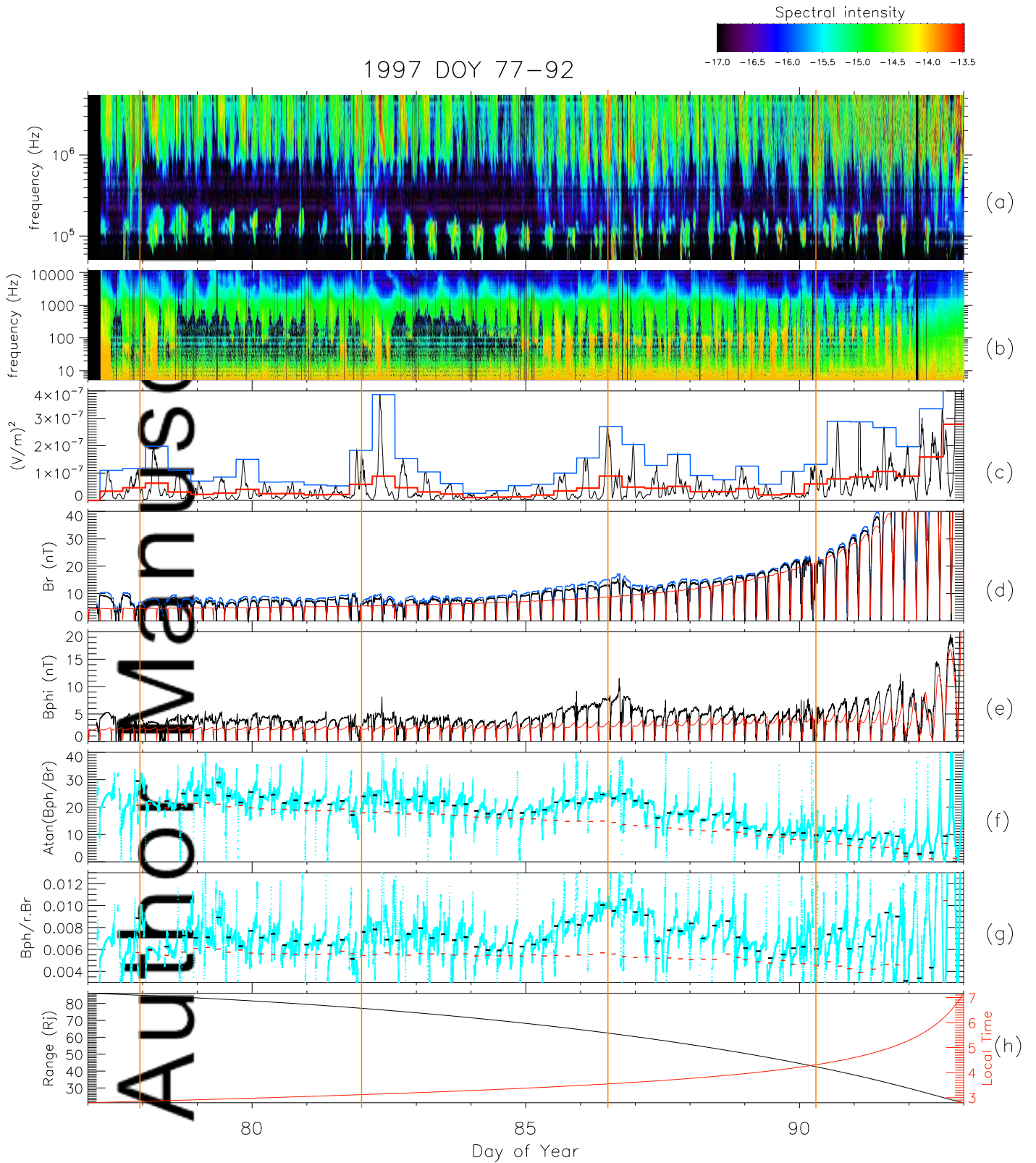


FIGURE 3

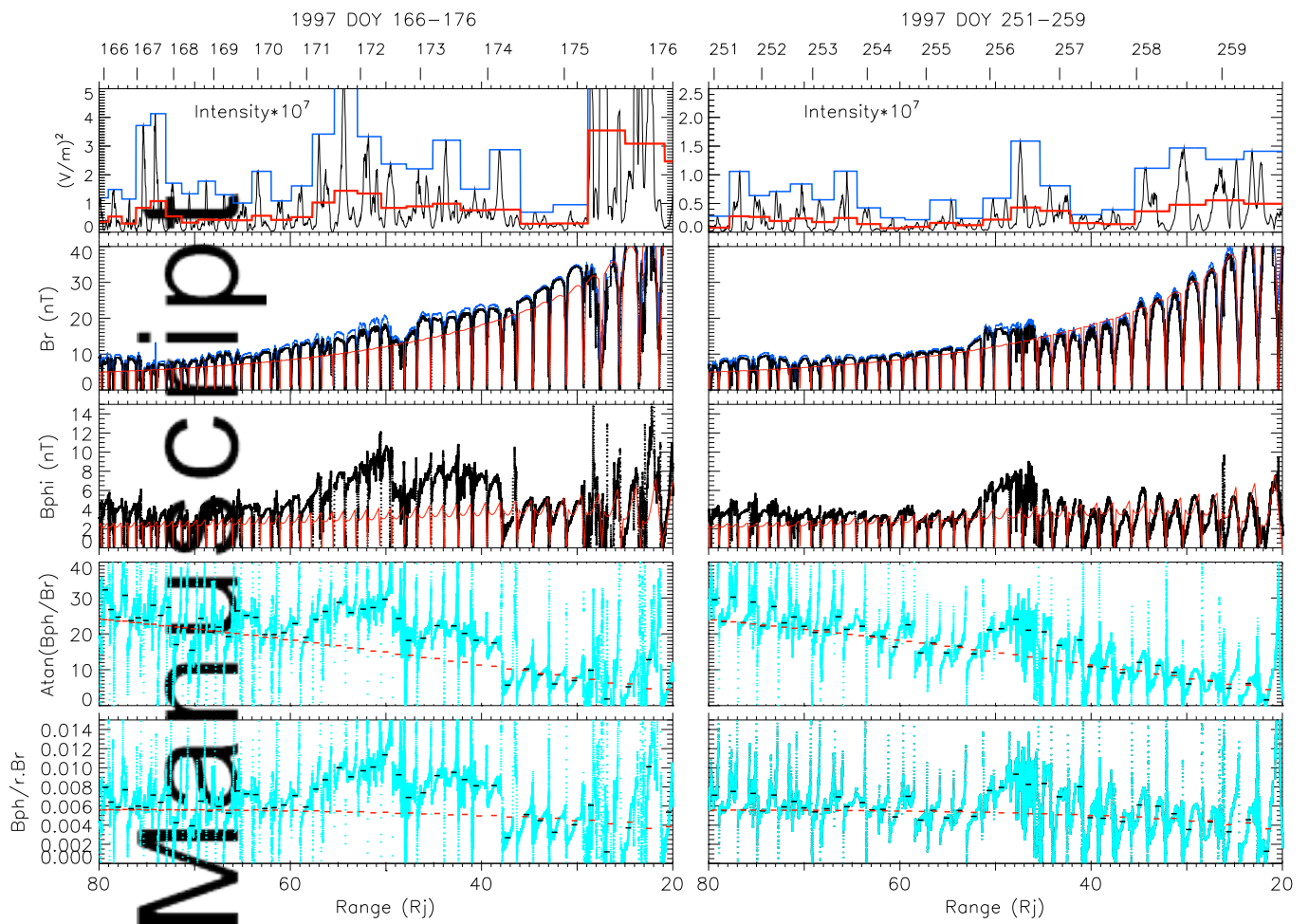


FIGURE 4

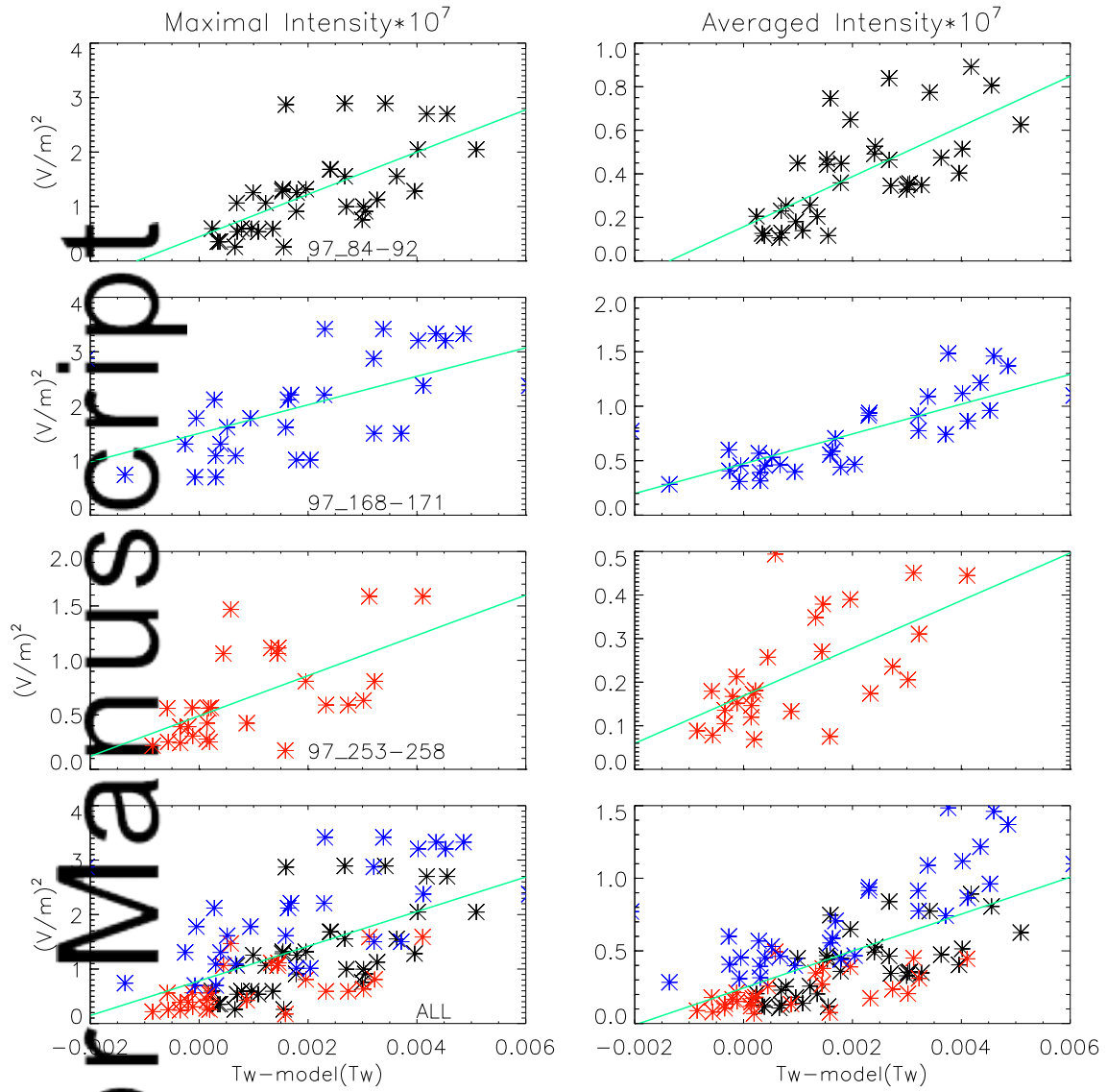


FIGURE 5

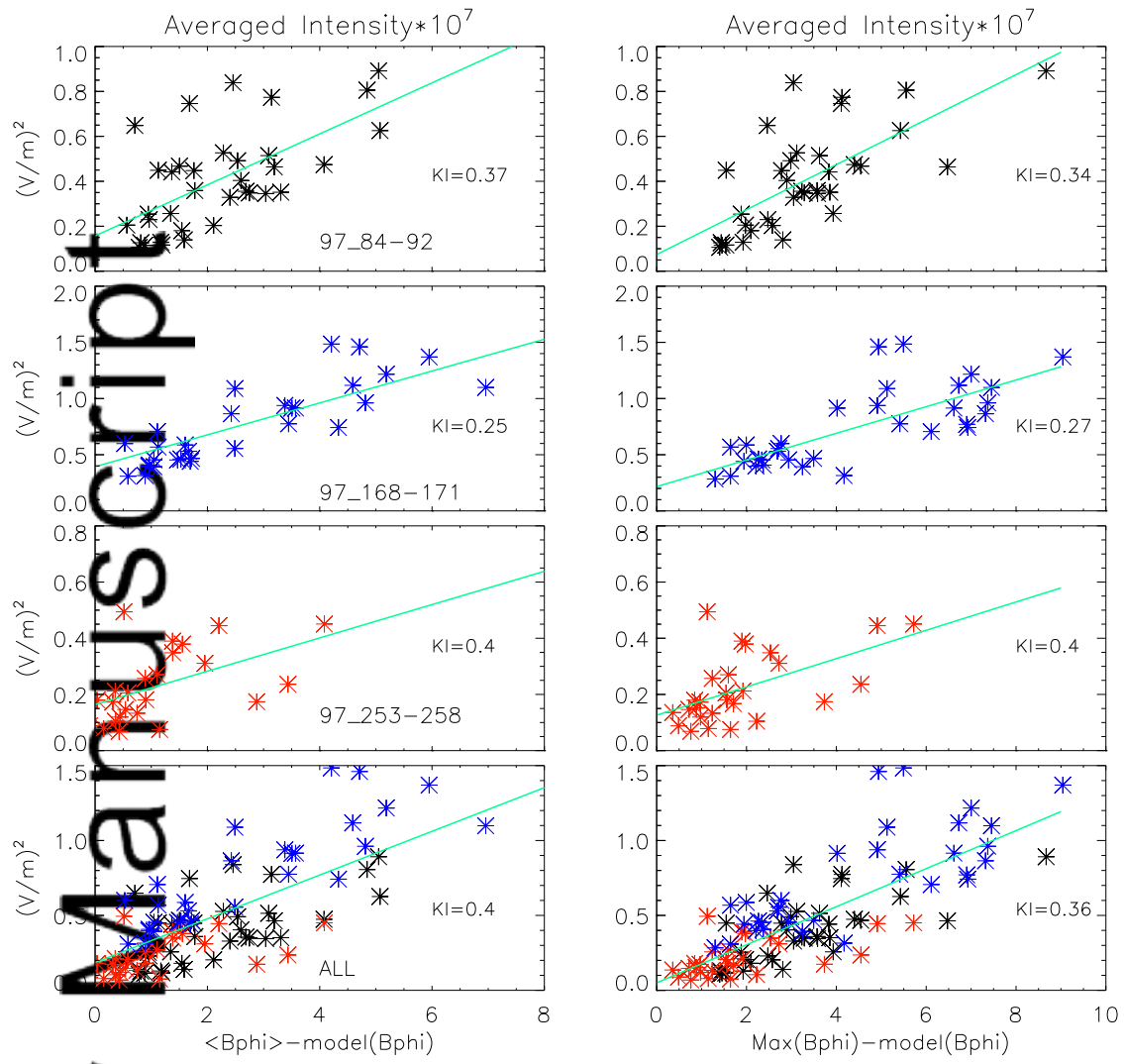


FIGURE 6

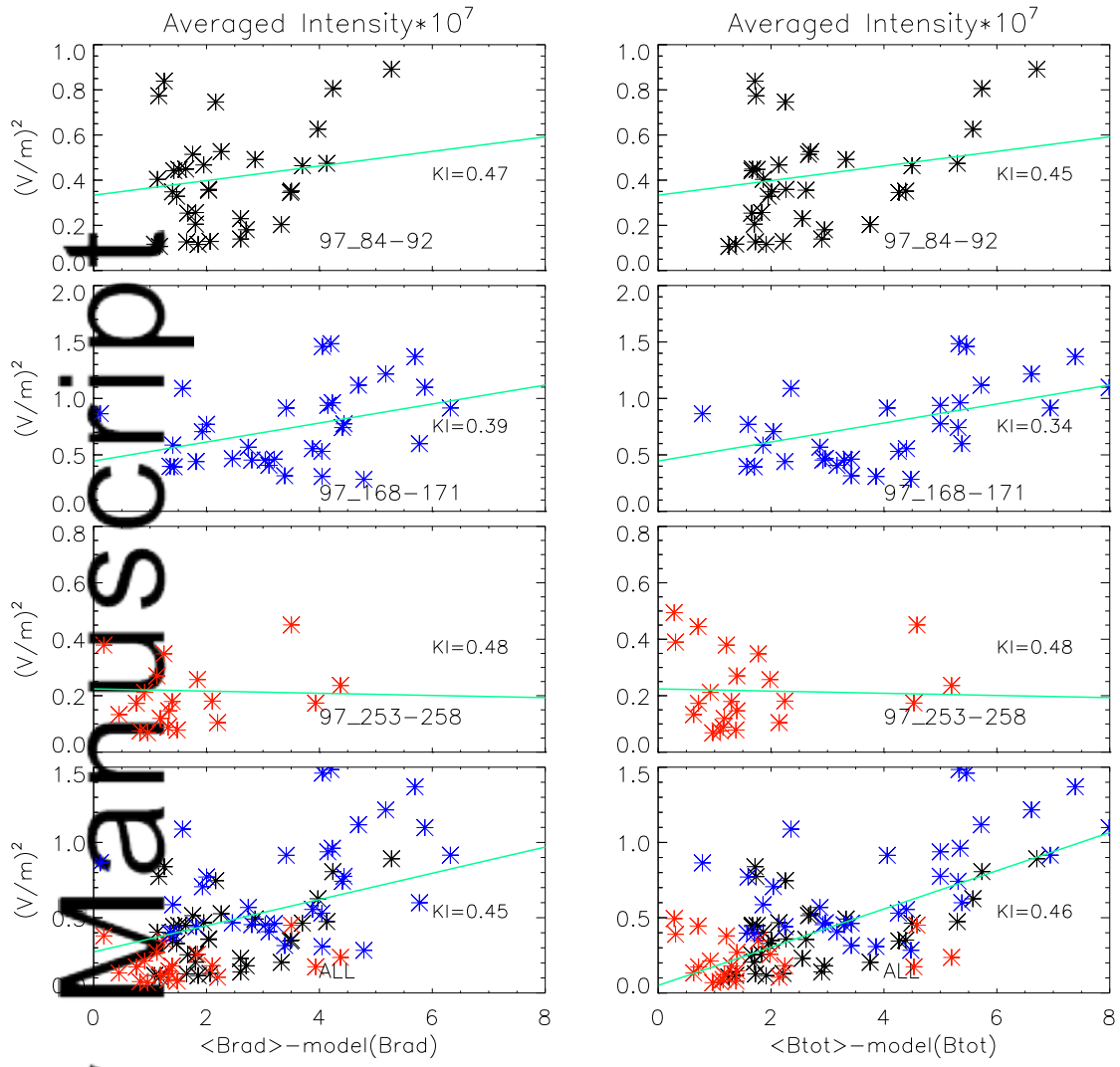


FIGURE 7

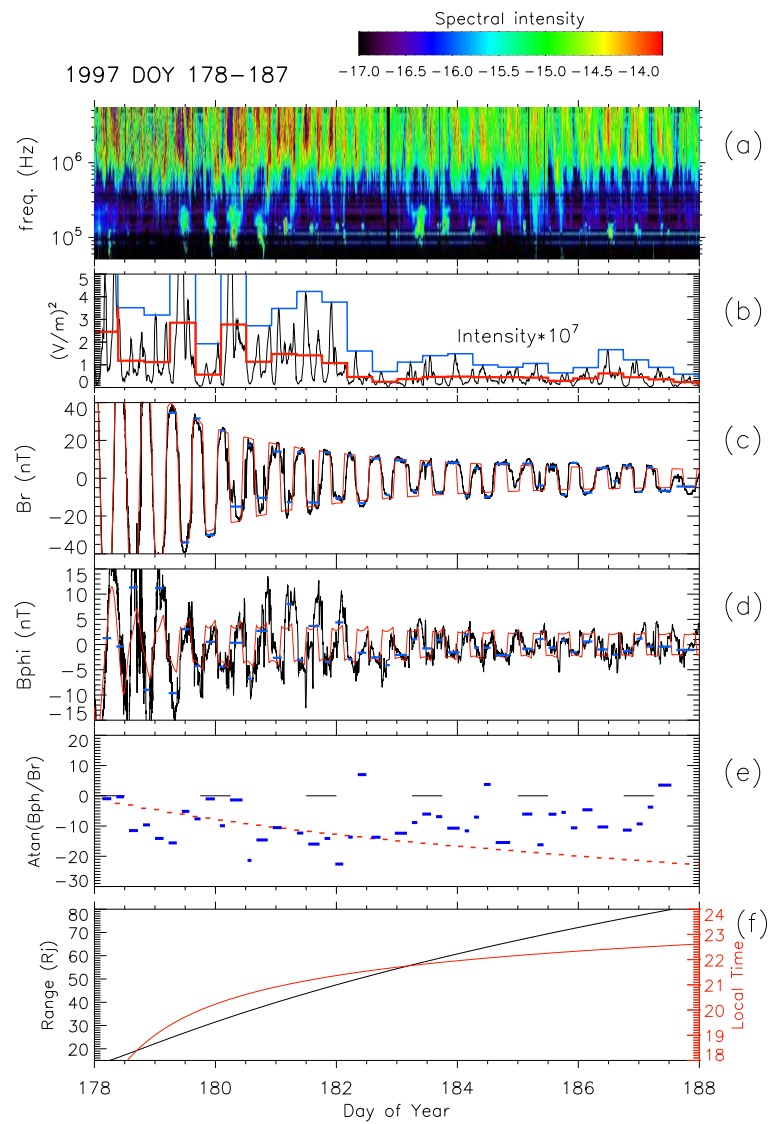


FIGURE 8

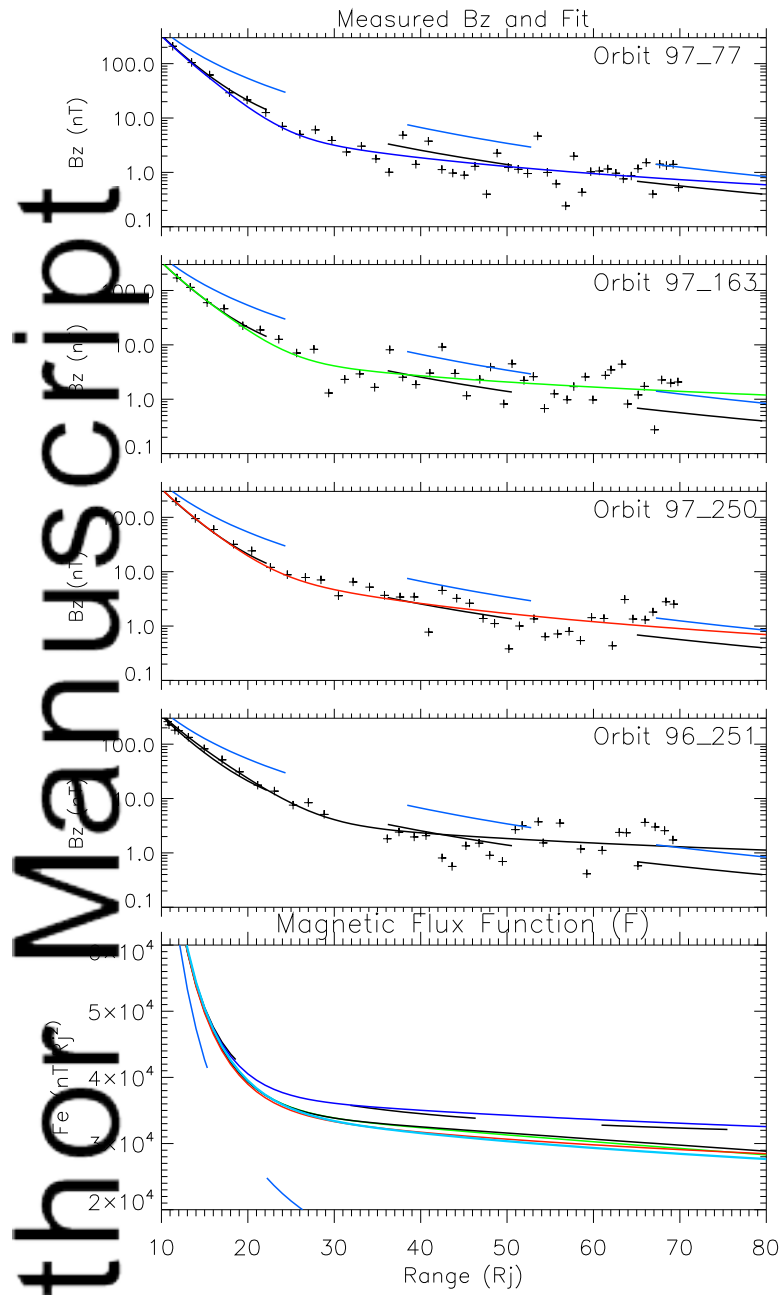


FIGURE 9

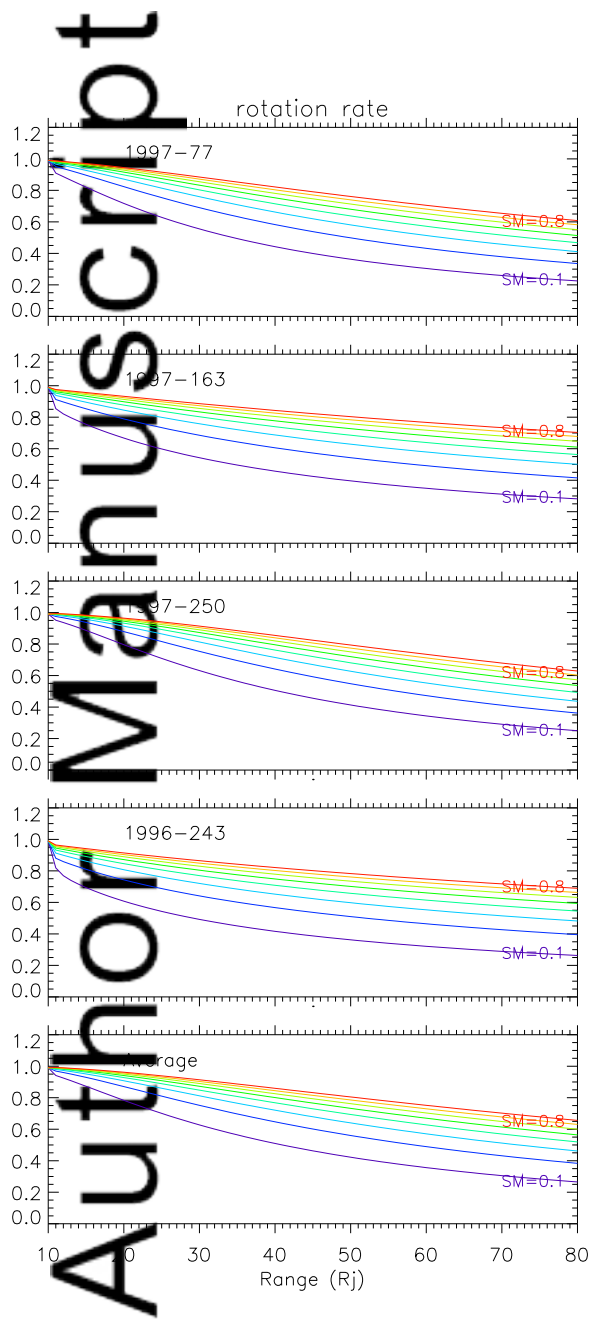


FIGURE 10

